The Astrophysical Journal, 923:130 (15pp), 2021 December 10 https://doi.org/10.3847/1538-4357/ac13a1

SOFIA Observations of 30 Doradus. I. Far-infrared Dust Polarization and Implications for Grain Alignment and Disruption by Radiative Torques

Le Ngoc Tram[1,5], Thiem Hoang[2,3], Enrique Lopez-Rodriguez[4], Simon Coudé[1], Archana Soam[1], B-G Andersson[1], Min-Young Lee[2], Lars Bonne[1], William D. Vacca[1], and Hyeseung Lee[2]

[1] Stratospheric Observatory for Infrared Astronomy, Universities Space Research Association, NASA Ames Research Center, MS 232-11, Moffett Field, CA 94035, USA; nle@mpifr-bonn.mpg.de

[2] Korea Astronomy and Space Science Institute, Daejeon 34055, Republic of Korea

[3] Korea University of Science and Technology, 217 Gajeong-ro, Yuseong-gu, Daejeon, 34113, Republic of Korea

[4] Kavli Institute for Particle Astrophysics and Cosmology (KIPAC), Stanford University, Stanford, CA 94305, USA

Received 2021 May 18; revised 2021 July 5; accepted 2021 July 6; published 2021 December 15

Abstract

Located in the Large Magellanic Cloud and mostly irradiated by the massive star cluster R136, 30 Doradus is an ideal target to test the leading theory of grain alignment and rotational disruption by RAdiative Torques (RATs). Here, we use publicly available polarized thermal dust emission observations of 30 Doradus at 89, 154, and 214 μm using SOFIA/HAWC+. We analyze the variation of the dust polarization degree (p) with the total emission intensity (I), the dust temperature ($T_{\rm d}$), and the gas column density ($N_{\rm H}$) constructed from Herschel data. The 30 Doradus complex is divided into two main regions relative to R136, namely North and South. In the North, we find that the polarization degree first decreases and then increases before decreasing again when the dust temperature increases toward the irradiating cluster R136. The first depolarization likely arises from the decrease in grain alignment efficiency toward the dense medium due to the attenuation of the interstellar radiation field and the increase in the gas density. The second trend (the increase of p with $T_{\rm d}$) is consistent with the RAT alignment theory. The final trend (the decrease of p with $T_{\rm d}$) is consistent with the RAT alignment theory only when the grain rotational disruption by RATs is taken into account. In the South, we find that the polarization degree is nearly independent of the dust temperature, while the grain alignment efficiency is higher around the peak of the gas column density and decreases toward the radiation source. The latter feature is also consistent with the prediction of rotational disruption by RATs.

Unified Astronomy Thesaurus concepts: Interstellar dust extinction (837); Interstellar clouds (834); Interstellar dust (836); Interstellar objects (52); Starlight polarization (1571)

1. Introduction

Grain alignment induces the polarization of background starlight and of thermal dust emission. Dust polarization induced by aligned dust grains is widely used to map magnetic fields (see, e.g., Lazarian 2007). A leading theory describing grain alignment is based on RAdiative Torques (hereafter RATs), which arises from the interaction of an anisotropic radiation field with irregular dust grains (Dolginov & Mytrophanov 1976; Draine & Weingartner 1996; Lazarian & Hoang 2007; see Andersson et al. 2015; Lazarian et al. 2015 for recent reviews). According to the RAT alignment theory, the alignment efficiency of dust grains depends on the radiation field and the local gas properties (e.g., Hoang et al. 2021; Soam et al. 2021a). Gas collisions tend to damp the grain rotation and randomize the grain orientation, whereas RATs act to spin up and align dust grains. Therefore, toward the center of a dense cloud, the degree of grain alignment by RATs decreases due to the attenuation of the interstellar radiation field (ISRF) and the increase in gas density. This results in the decrease of the dust polarization degree (p) toward the center of molecular clouds (MCs), i.e., toward higher gas column density $N_{\rm H}$ (see, e.g., Hoang et al. 2021). Numerous observations toward MCs report a decrease in the polarization degree with $N_{\rm H}$, which favors the RAT alignment theory (Whittet et al. 2008; Alves et al. 2014; Vaillancourt et al. 2020). Note that the tangling of magnetic fields is also suggested to produce a decrease in polarization with increasing $N_{\rm H}$ (e.g., Jones et al. 1992).

With the advances in high-resolution polarimetric facilities (JCMT/POL2, ALMA, SOFIA/HAWC+), one can now observe the polarization induced by dust grains in the proximity of an embedded source (e.g., a protostar) where the effect of stellar radiation becomes dominant over that of the ISRF. As a result, toward the embedded source, the RAT alignment theory predicts the increase of the dust polarization with increasing radiation emission intensity (or dust temperature $T_{\rm d}$; Hoang et al. 2021). Numerical modeling (Lee et al. 2020) and numerical simulations (Reissl et al. 2016) of dust polarization using the RAT alignment theory report a monotonic increase in the polarization degree of thermal dust emission with increasing radiation intensity (or $T_{\rm d}$). Such a correlation of p with $T_{\rm d}$ is an important feature predicted by the RAT alignment theory. As a result, observing dust polarization around a strong radiation source is crucial to test the RAT alignment theory (see, e.g., Medan & Andersson 2019; Soam et al. 2021b).

Interestingly, polarimetric observations reveal that the degree of thermal dust polarization does not always increase with radiation intensity (or dust temperature, $T_{\rm d}$) and decrease with increasing $N_{\rm H}$, as implied by the RAT alignment theory. For example, Planck observations at 850 μm toward four molecular clouds, including Aquila Rift, Cham-Musca, Orion, and Ophiuchus in the Gould Belt cloud, showed that the polarization degree decreases for $T_{\rm d} > 19$ K (see Planck Collaboration et al. 2020).

[5] Current address: Max-Planck-Institut für Radioastronomie, Auf dem Hügel 69, 53-121, Bonn, Germany.

Shorter-wavelength polarimetric measurements at 500 μm from the air-balloon BLASTPol toward Vela C also show a similar decrease at $T_{\rm d} \geqslant 19$ K (see Fissel et al. 2016). Further shorter-wavelength observations by the High-resolution Airborne Wide band Camera Plus (HAWC+) instrument (Harper et al. 2018) aboard the Stratospheric Observatory for Infrared Astronomy (SOFIA) toward the molecular cloud Ophiuchus A at 89 and 154 μm also reported a decrease in the polarization degree for $T_{\rm d} \geqslant 25$–32 K and $N \leqslant 10^{22}$ cm^{-2} (see Santos et al. 2019 and Tram et al. 2021a). For the case of ρ Ophiuchus A, the peak of the dust temperature is close to the central source (a B-association star), while the gas column density peaks farther away. Thus, the decrease in the dust polarization degree toward high dust temperatures and low gas densities (toward the source) could not be explained by the loss of grain alignment due to weak radiation intensity or enhanced collisional randomization as in the case of starless cores (Whittet et al. 2008; Alves et al. 2014).

Hoang et al. (2019) realized that large grains cannot survive once exposed to a strong radiation field owing to the Radiative Torque Disruption (RATD) mechanism (see Hoang 2020 for a review). The RATD mechanism causes the large grains to fragment into many smaller species when the centrifugal stress induced by suprathermal rotation due to RATs exceeds the tensile strength of the grain material, which is determined by the binding energy that holds their constituents together. RATD is more efficient for large grains because the RAT efficiency increases with grain size (Lazarian & Hoang 2007; Hoang & Lazarian 2008). The depletion of large grains due to RATD is expected to result in the decrease of the polarization degree of the thermal dust emission because large grains dominate the polarized emission at long wavelengths.

The first numerical modeling of dust polarization that considers both grain alignment and rotational disruption by RATs was performed by Lee et al. (2020). They found that the dust polarization degree increases monotonically with $T_{\rm d}$ when grains are aligned by RATs and the RATD effect is not taken into account. In the presence of RATD, the polarization degree first increases and then decreases when the dust temperature becomes sufficiently large (i.e., the corresponding radiation strong enough) to activate the RATD effect. The critical temperature for the RATD effect depends on the local gas density and grain tensile strength that depends on the grain structure. Their modeling results could successfully reproduce the anticorrelation $p-T_{\rm d}$ trend at 850 μm observed by Planck (Planck Collaboration et al. 2020). As a result, the variation of p with $T_{\rm d}$ observed toward an intense radiation source becomes an important test for the RAT alignment and RATD theory. The first detailed analysis of the $p-T_{\rm d}$ relation is carried out in Tram et al. (2021a) for the SOFIA/HAWC+ observations from Ophiuchus A cloud at 89 and 154 μm. The authors found that $p-T_{\rm d}$ is anticorrelated at sufficiently large $T_{\rm d}$ and showed that it could be reproduced by RAT alignment and RATD mechanism. Ngoc et al. (2021) also found the anticorrelation of $p-T_{\rm d}$ toward the proximity of the LkHα 101 star in the Auriga-California cloud. These studies reveal the importance of RATD that needs to be taken into account together with RAT alignment to interpret dust polarization data observed toward an intense radiation source. Moreover, observational data also allow us to constrain the physical properties and characteristics of dust grains, such as shape, internal structure, mineralogy, helicity, and size distribution.

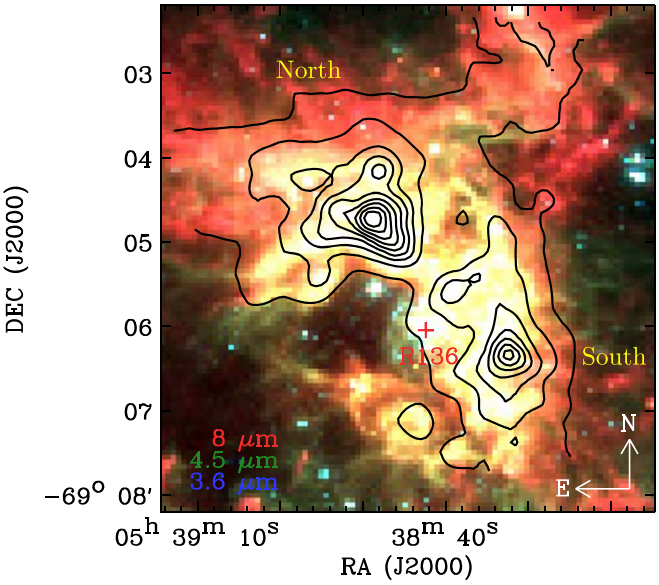

Figure 1. An RGB composite image of 30 Doradus with R: 8 μm, G: 4.5 μm, and B: 3.6 μm. The black contours show an example of the FIR observations at 154 μm with SOFIA/HAWC+. There are two main regions in 30 Dor, North and South, relative to the massive star cluster, R136. The data analyzed in this work are located in the strong radiation field.

In this paper, we will use the thermal dust polarization observed by SOFIA/HAWC+ at 89, 154, and 214 μm toward a massive star-forming cloud, 30 Doradus (hereafter 30 Dor) to test the RAT alignment and RATD mechanism. 30 Dor is located in the Large Magellanic Cloud (LMC) at the distance of $\sim$50 kpc from us (e.g., De Marchi et al. 2011) and powered by the massive star cluster R136, with a mass of $\simeq 5 \times 10^4 M_\odot$ (see Indebetouw et al. 2009 and references therein) and the bolometric luminosity of $7.8 \times 10^7 L_\odot$ (see Lopez et al. 2011 and references therein). Note that the LMC is a low-metallicity galaxy ($Z \simeq 0.5 Z_\odot$, Dufour et al. 1982; Galliano et al. 2008; Chevance et al. 2016), with a low dust-to-gas ratio (e.g., $\sim$2–5 $\times 10^{-3}$; see Roman-Duval et al. 2014; Chevance et al. 2016), which makes the dust shielding relatively low such that dust grains can be affected by the radiation field over a large scale (see Figure 1). Thus, the 30 Dor cloud offers a valuable environment to test the physics of grain alignment and disruption by RATs. Toward this end, we will concentrate on the correlation of the polarization degree with the emission intensity, the dust temperature, and the gas column density.

This paper is structured as follows. We first present the FIR polarimetric observations of 30 Dor observed by SOFIA/HAWC+ in Section 2. We then present (1) the distribution of the polarization angle and the polarization degree, (2) the relation of the polarization degree with the total intensity, the gas column density, and dust temperature in Section 3. The implications of the observational data for grain alignment and rotational disruption by RATs are presented in Section 4. The summary of our main findings is presented in Section 5.

2. Observations of 30 Doradus

2.1. SOFIA/HAWC+ Multiwavelength Polarization

Polarization of thermal dust emission from 30 Dor was observed by SOFIA/HAWC+ at three bands: C at 89 μm, D at 154 μm, and E at 214 μm. The beams sizes (FWHM) are 7.″8, 13.″6, and 18.″2 at 89 μm, 154 μm, and 214 μm, respectively.

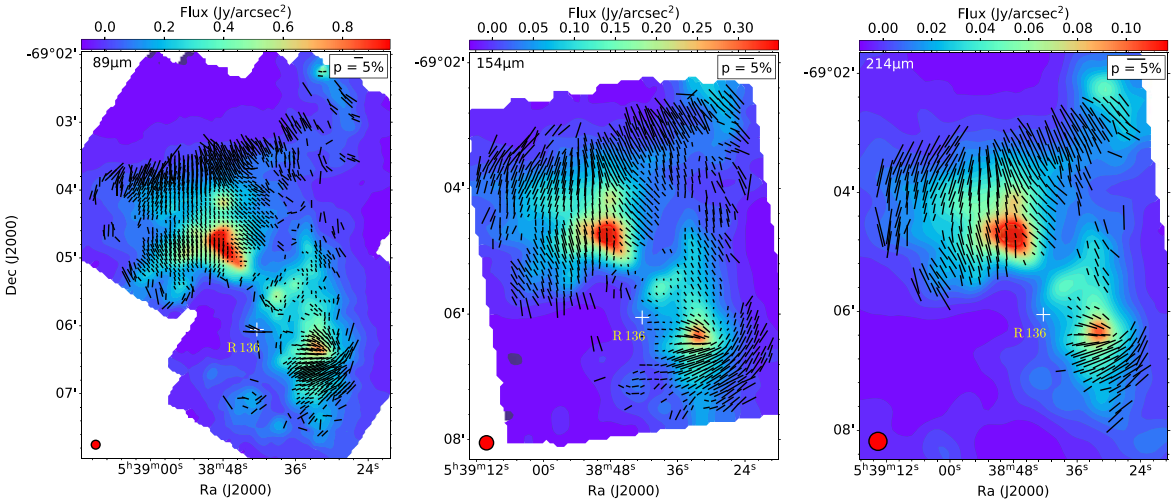

Figure 2. Polarization maps (E vectors) of 30 Dor observed using SOFIA/HAWC+ at 89 (left), 154 (middle), and 214 μm (right). The background color is the total intensity (Stokes I). The vectors are selected within the thresholds of $I/\sigma_I \geqslant 100$ and $p/\sigma_p \geqslant 3$ (see Section 2.1). The beam size (red circle) at the respective wavelengths and a 5% polarization measurement (top right) are shown. The location of R136 (white cross) is shown in every panel.

Data are publicly available under the Strategic Director's Discretionary Time (S-DDT) program (PI: Yorke, H., ID: 76_0001); the observations were taken during the SOFIA New Zealand deployment in 2018 July. Data have been presented by Gordon et al. (2018) and no further data reduction has been performed.

For the linear polarization, the polarized intensity is defined as (Gordon et al. 2018)

$$I_p = \sqrt{Q^2 + U^2}, \tag{1}$$

with Q the Stokes parameter Q, U the Stokes parameter U. The association error is then

$$\sigma_{I_p} = \left[\frac{(Q\sigma_Q)^2 + (U\sigma_U)^2}{Q^2 + U^2}\right]^{1/2}, \tag{2}$$

with σ_Q the error of Stokes Q and σ_U the error of Stokes U.

The debiased polarization degree is calculated as

$$p = \frac{100}{I}\sqrt{Q^2 + U^2 - \sigma_{Ip}^2} = 100\frac{I_p}{I} \quad (\%), \tag{3}$$

with I the Stokes I parameter. The associated error is then

$$\sigma_p = p\left[\left(\frac{\sigma_{I_p}}{I_p}\right)^2 + \left(\frac{\sigma_I}{I}\right)^2\right]^{1/2} \tag{4}$$

with σ_I the error of Stokes I.

Finally, the polarization angle and its error are given by

$$\theta = \frac{1}{2}\arctan\left(\frac{U}{Q}\right) \tag{5}$$

and

$$\sigma_\theta = \frac{1}{2}\frac{\sqrt{(Q\sigma_U)^2 + (U\sigma_Q)^2}}{Q^2 + U^2}. \tag{6}$$

We then performed quality cuts to obtain statistically significant polarization measurements. The quality cuts on the polarization map are very conservative. In this work, we mask our HAWC+ maps by using two common thresholds. The first quality cut depends on the signal-to-noise ratio of Stokes I (I/σ_I); we adopt $I/\sigma_I \geqslant 100$, which allows $\sigma_p \simeq \sqrt{2} \times (I/\sigma_I)^{-1} = 1.4\%$.[6] The second threshold is the signal-to-noise ratio of the polarization degree $p/\sigma_p \geqslant 3$. Figure 2 shows the final map of the polarization vectors (E vectors, not B vectors). The length of the polarization measurements is referenced to 5% of the polarization degree. Data for band C (89 μm), D (154 μm), and E (214 μm) are shown from left to right, and the background color is the original total intensity (Stokes I). Figures 3(a) and (c) show the final maps of Stokes I and the polarization degree at 214 μm as an example. The correlations with the gas column density and the Stokes I are visualized by the black contours.

2.2. Gas Column Density and Dust Temperature

We constructed the maps of dust temperature, T_d, and the gas column density, $N_H \simeq N(H + H_2)$, using Herschel data at 100, 160, 250, 350, and 500 μm from HERITAGE (Meixner et al. 2013). The observations were registered and sampled to 160 μm with a pixel scale of 3″ and FWHM = 11.″4, then a modified blackbody function was used to fit each of the line-of-sight (LOS) SEDs with an assumed spectral index of $\beta = 1.62$. This value was taken as the median from the range of $\beta \sim 1.5$–1.8 by Gordon et al. (2014) and $\beta = 2.0$ used by Bernard et al. (2008).

Panels (b) and (d) in Figure 3 show the maps of the gas column density and dust temperature in 30 Dor. Toward R136, the dust temperature increases, while the gas column density first increases and then decreases after its peak, which is farther away from the center. The correlations are visualized by the black contours in these maps. In addition, the dust temperature (gas column density) in the North is hotter (denser) than that in the South.

3. Results

We now show the results analyzing the polarization degree of thermal dust emission in 30 Dor in terms of the total emission intensity, dust temperature, and gas column density.

[6] This approximation is derived from Equation (4) by assuming that $\sigma_Q = \sigma_U$.

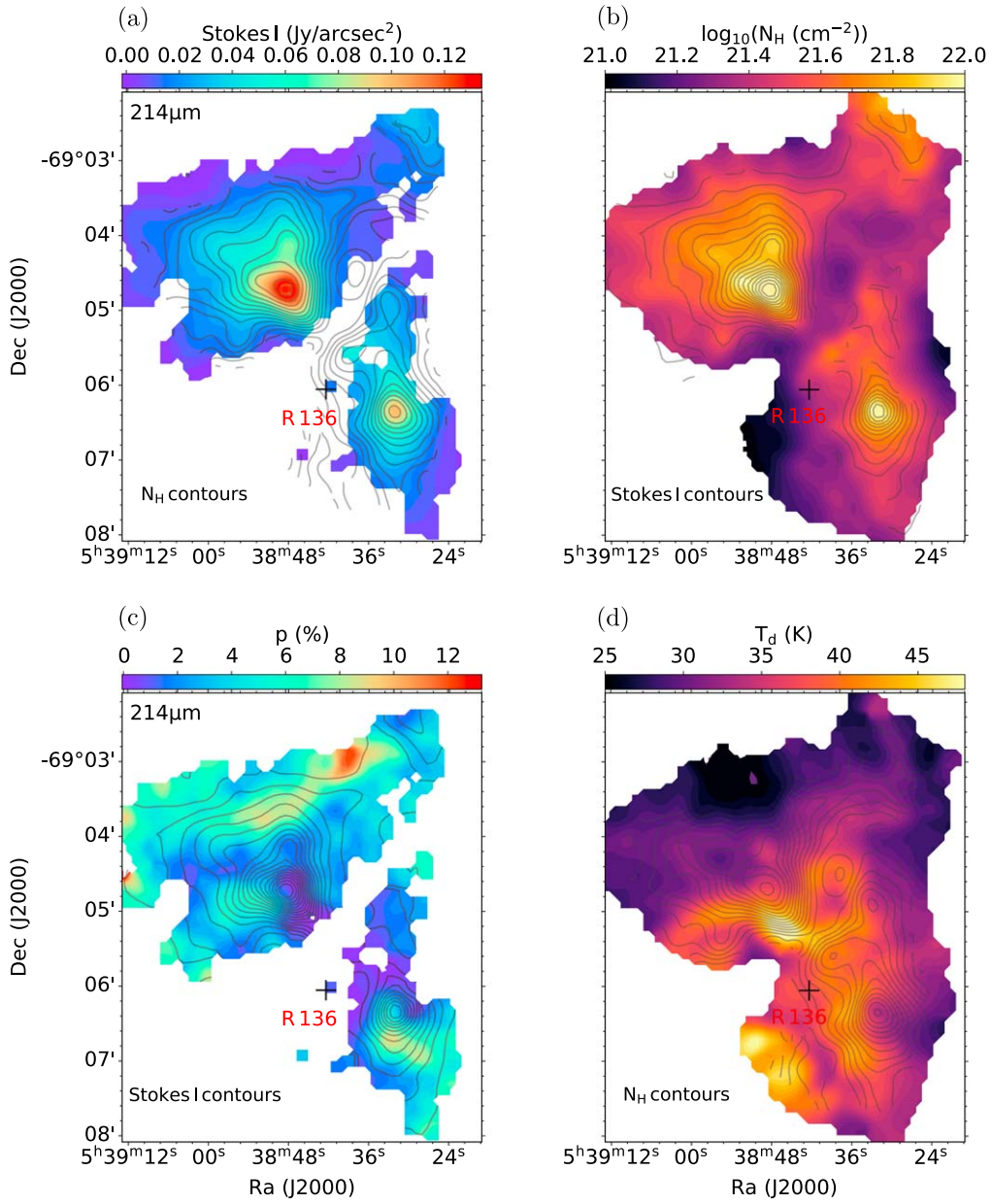

Figure 3. Panels (a) and (c): maps of the total intensity and the polarization degree at 214 μm after masking from the common sky positions in which all three bands in Figure 2 detected the signal. Panels (b) and (d): maps of the gas column density and the dust temperature. The black cross shows the location of the massive star cluster R136. The total intensity correlates well with the gas column density. The gas column density peak is offset from the dust temperature, whose peak is close to R136.

3.1. Variation of the Polarization in 30 Dor

The upper panels in Figure 4 show the distribution of the polarization angle of the thermal dust polarization in 30 Dor at three bands. We chose to use a position angle span of $-90°$ to $+90°$ to center the position angles around the peak of the distribution. The variation of the polarization angle is very similar for the three bands. The distributions of all vectors are shown by the cyan area, which shows that the polarization vectors vary quite significantly, spanning from $-90°$ to $90°$, and peak at around $20°$ and $-60°$. The first peak is characterized by polarization in the North (see the red distribution). The second peak originates predominantly in the South (see the blue distribution), which has a more random statistic. These distributions have the same bin width, which is chosen following the Freedman–Diaconis rule in the Python package[7] from all vectors. The weighted-mean values and the uncertainties have been calculated as shown by the dashed vertical thick and corresponding thin lines, whose values are listed in Table 1.

The lower panels in Figure 4 show the distribution of the polarization degree in three bands. The distribution peaks between 2% and 4%. The red and blue histograms show the distributions in the North and South, respectively. The choice of bin width is the same as above. The weighted mean and the associated 1σ uncertainties are shown by the dashed vertical thick and thin lines, whose values are also listed in Table 1.

[7] https://docs.astropy.org/en/latest/visualization/histogram.html

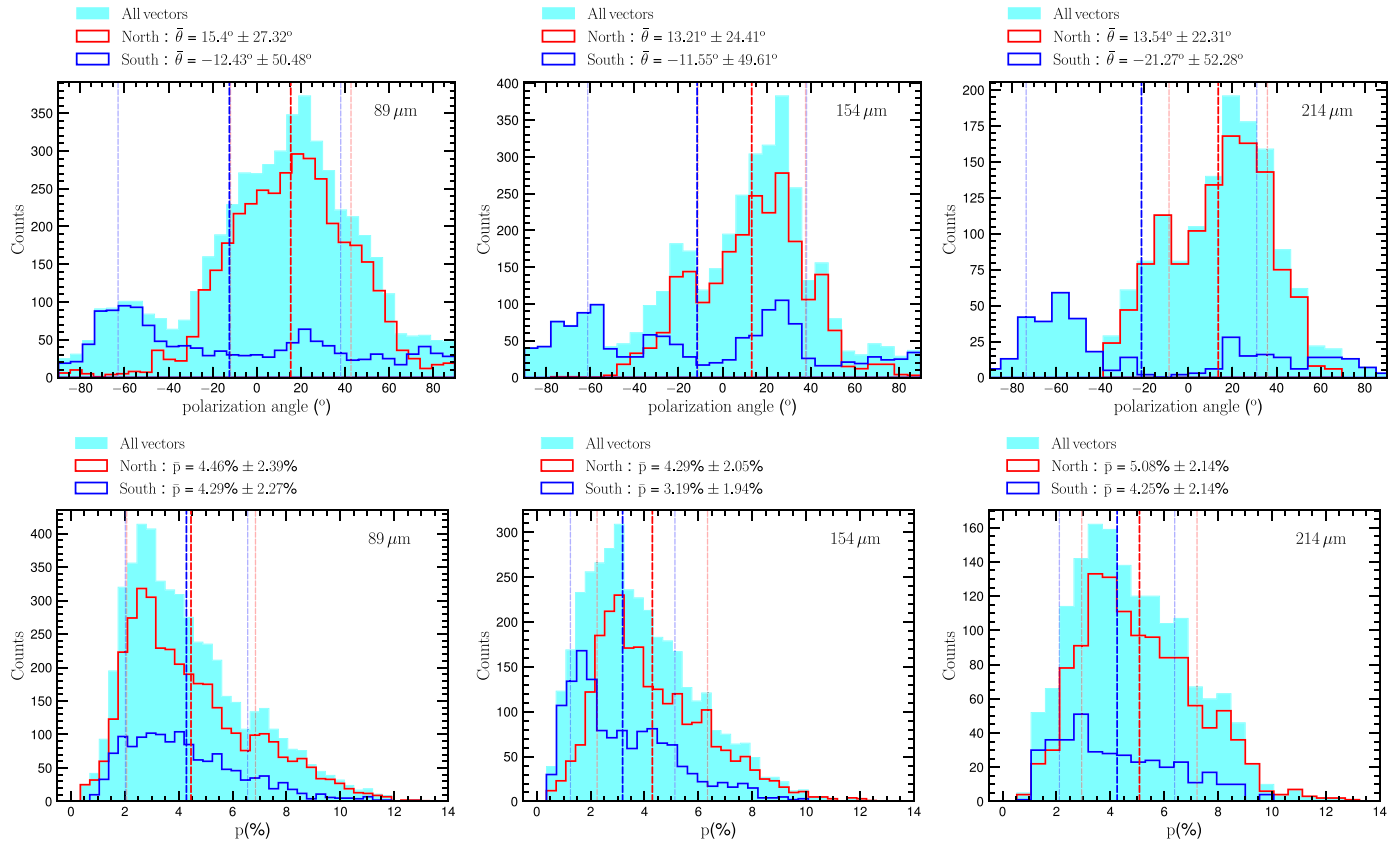

Figure 4. Distribution of the polarization angle (upper panels) and the polarization degree (lower panels) in three bands (from left to right). Cyan, red and blue are the distributions of the polarization measurement in the entire region, in the North and in the South regions (see Figure 2), respectively. The vertical dashed red and blue lines are the weighted means of the North and the South distributions. The corresponding thinner lines represent the 1σ uncertainties.

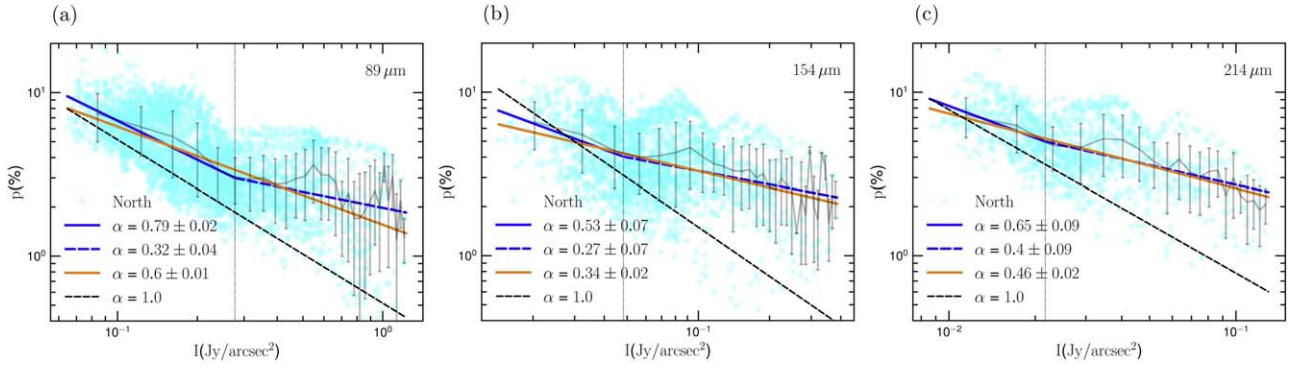

Figure 5. Relation of the polarization degree and the total intensity in three bands in the North region. The gray error bars are the weighted means within the bins of each data. A single power-law fitting is shown by the orange line, while the blue line is for a double power law. In the latter case, the transitions are shown by the dashed vertical lines. As a comparison, the power law with $\alpha = 1$ is shown by the dashed black line.

Table 1
Mean Value and Uncertainties of the Polarization Angle (θ) and the Polarization Degree (p) in the North and South Regions in Three Bands

Bands	$\theta^o(\pm1\sigma)$		$p(\%)(\pm1\sigma)$	
	North	South	North	South
89 μm	15.4(27.32)	−12.43(50.48)	4.46(2.39)	4.29(2.27)
154 μm	13.21(24.41)	−11.55(49.61)	4.29(2.05)	3.19(1.94)
214 μm	13.53(22.31)	−21.27(52.28)	5.08(2.14)	4.25(2.14)

Notably, the σ is larger than the maximum associated uncertainty of 1.4%, thus the 1σ is intrinsically associated with changes in the source.

3.2. Polarization Degree versus Total Intensity

Figure 5 shows the relation of the polarization degree to the total intensity for all three bands in the North region. We first fit the observational data with a single power-law function (solid orange line) using the LMFIT Python package (Newville et al. 2014) and compare it with the limiting case of $\alpha = 1$ (black

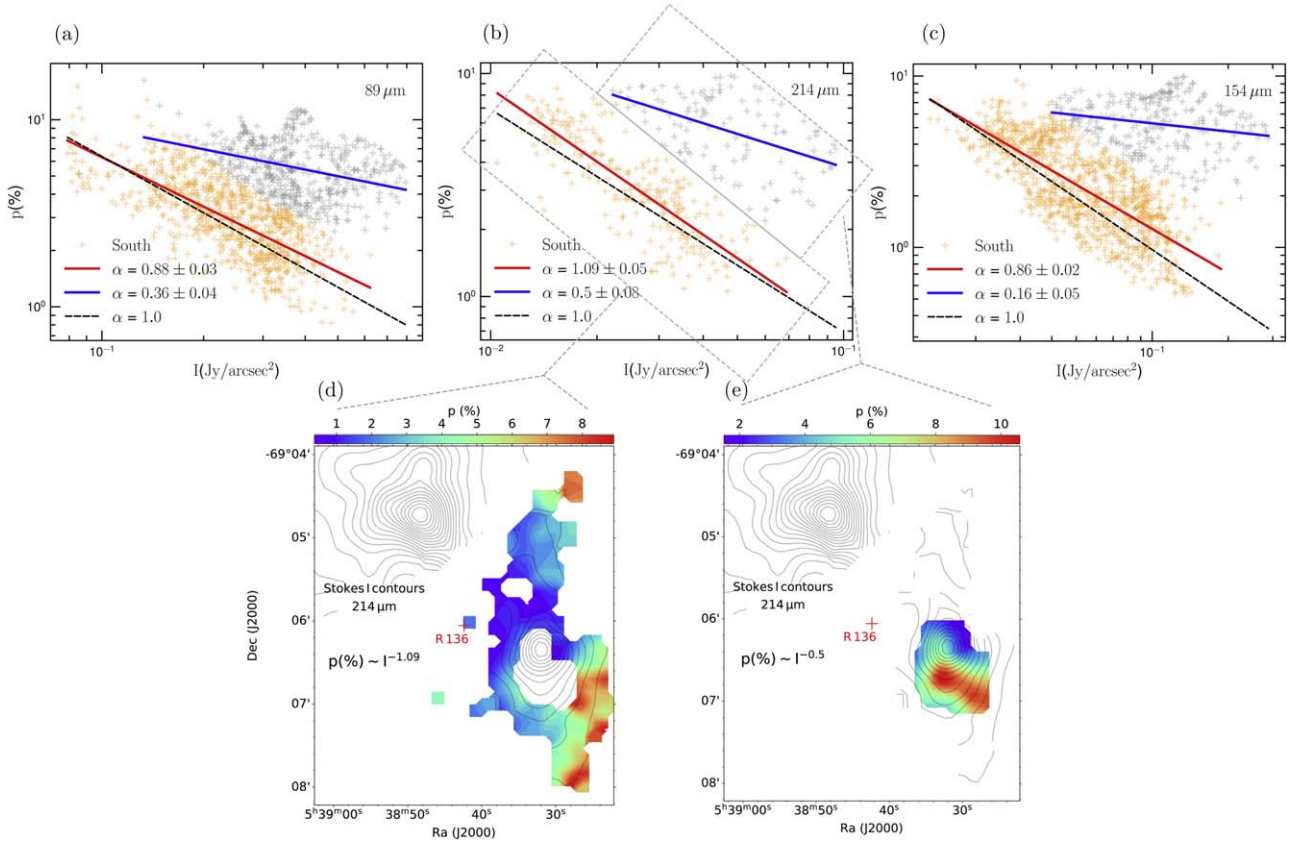

Figure 6. Similar to Figure 5 but for the South. The data points likely group separately, hence we classify them into two different clusters by using the BAYESIANGAUSSIANMIXTURE library in the Python package. These clusters are shown by the gray and orange points in panels (a)–(c), which are followed by the power-law fittings. The slope differs from one cluster to another, which indicates a different grain alignment efficiency between the two regions. Panels (d) and (e) visualize the spatial distribution of these clusters. The slope is shallower around the peaked intensity and gas column density, whereas the polarization decreases steeply to higher intensity.

dashed line). The best fit indicates the slope of $\alpha = 0.6 \pm 0.01$ at 89 μm is steeper than 0.5 (in the case the medium is fully turbulent, Jones et al. 1992) and the estimated slopes at 154 μm ($\alpha = 0.34 \pm 0.02$) and 214 μm ($\alpha = 0.46 \pm 0.02$). We then fit the data with a double power-law function (solid and dashed blue lines) using the piecewise linear least-squares fit PWLF (Jekel & Venter 2019). The best fits illustrate two distinct slopes, whose transitions are marked by the dashed–dotted vertical lines. The transitions occur at 0.28 ± 0.02 Jy arcsec^{-2}, 0.05 ± 0.01 Jy arcsec^{-2}, and 0.02 ± 0.003 Jy arcsec^{-2} at 89 μm, 154 μm, and 214 μm, respectively. In this case, as the intensity increases, the polarization degree first declines rapidly with a steep slope of $\alpha > 0.5$ (solid blue line) and then varies with a shallow slope with $\alpha < 0.5$ (dashed blue line). The first steep slope is still shallower than the $\alpha = 1$ predicted by the model in which grains are only aligned in the outer envelope of the cloud (see, e.g., Hoang et al. 2021). We note that the slope difference gets smaller for longer wavelengths.

Figure 6 shows the relation of the polarization degree to the total intensity for all three bands in the South region (panels a, b, and c). The relations are complex, but the data appear to group into two different clusters. We then used the BAYESIANGAUSSIANMIXTURE library in the SCIKIT-SKLEARN Python package (Pedregosa et al. 2011) to classify the data points into two groups. Because the separation at 89 μm is less obvious than that at 154 and 214 μm, the classification works well at these longer wavelengths and fails at 89 μm. Thus, to make it consistent, we classify this case into three groups then merge two of them together. Each cluster is plotted in a different color and is fitted by a power law, as shown in the legend. The polarization degree is higher, and the slope is steeper from one cluster to another.

To better understand the observed features, we show in panels (e) and (d) of Figure 6 the spatial positions of these two clusters at 214 μm as an example. The central region (colored area in panel e) seems to be shielded partially from the irradiation of R136, whereas the outer region (colored area in panel d) contains a near-side region that is directly irradiated by the source R136. Surprisingly (also differing from the North), the high polarization degree and shallower slope of the $p-I$ diagram are seen for the central region, located around the intensity peak (or the gas column density peak; see Figure 3(a)). Moreover, the polarization degree in the near-side region (close to R136) is much lower than that in the far-side region (lower- and upper-right corners; see color bars). The low polarization degree at higher radiation intensity is unexpected from the basic RAT alignment theory.

We note that the best fits to the $p-I$ data only reflect the general trend and cannot describe accurately the underlying physics across the different regions. Indeed, as shown in Figure 5, there are many data points that appear to follow the steep slope of $\alpha = 1$ toward high intensity. This can also be seen from Figure 3(c) that the polarization degree is minimum around the central radiation source, while it becomes higher at

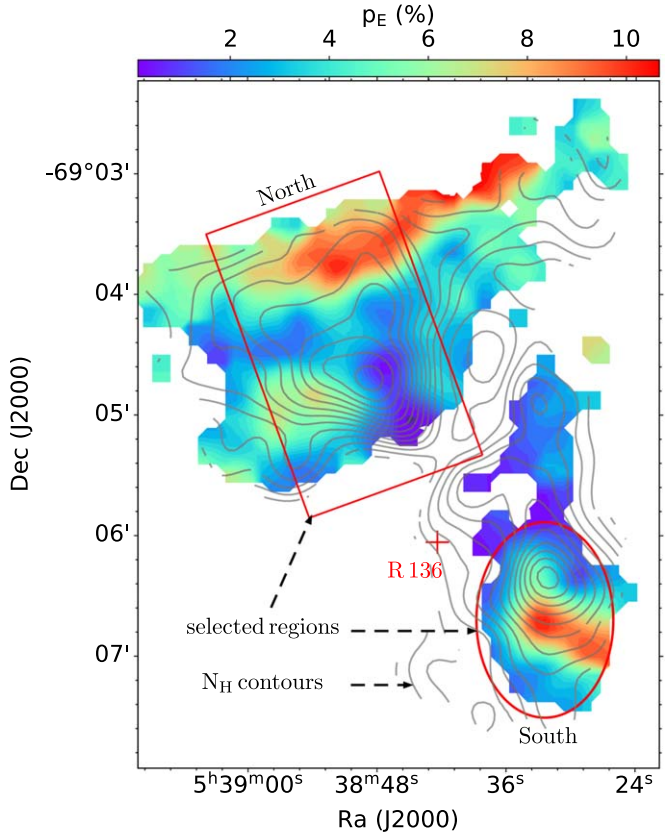

Figure 7. Subregion selections. The background is the polarization degree at band E of the common space position where SOFIA/HAWC+ detected data in all three bands. The contours show the gas density map. The red rectangle (origin at $5^{h}38^{m}51\overset{s}{.}041$ $-69°04'25\overset{''}{.}084$, width = $17\overset{s}{.}12$, height = $2\overset{'}{.}5$) and ellipse (origin at $5^{h}38^{m}32\overset{s}{.}4$ $-69°06'42''$, major axis = $6\overset{s}{.}05$, minor axis = $0\overset{'}{.}81$) show the selected regions we are interested in.

the farthest side from this source where the dust temperature is relatively low (see Figures 3(b)–(d)). Therefore, in the next section, we will perform an additional analysis of the polarization with the gas column density and dust temperature.

3.3. Polarization Degree versus Dust Temperature and Gas Column Density

For the optically thin case, the total dust emission intensity is $I_\nu \propto B(T_d)\tau_\nu \sim \kappa_\nu N_H B(T_d) \times R$ with R the dust-to-gas ratio and κ_ν the dust opacity, which is the product of the gas column density and dust temperature along the line of sight. Therefore, the $p-I$ relation reflects the overall effect of both the radiation field and the gas density on grain alignment, assuming a uniform average magnetic field. To disentangle the effect of the radiation field from the gas density, we analyze the variation of the polarization degree with the dust temperature and the gas column density. The first analysis directly reveals the grain alignment and disruption by RATs, while the second one reflects the effect of grain randomization induced by gas collisions.

To make a comparison among the three bands, we first smooth the maps of the dust temperature, gas column density, and SOFIA/HAWC+ bands C and D to the $18\overset{''}{.}7$ FWHM, which is equivalent to the SOFIA/HAWC+ band E beam size. Then, we selected the common space position where three SOFIA/HAWC+ bands all detect data. The final map is shown in Figure 7. From this final map, we analyze the correlations in two subregions: within a rectangle in the North and within an ellipse in the South. These extraction areas, covering the representative features of both the gas density and the dust temperature in 30 Dor, are shown in Figure 7.

Figure 8 shows the two-dimensional histogram of the gas column density and the dust temperature relation for these two representative North (upper panel) and South (panel) regions. In the North, a PWLF fitting (Jekel & Venter 2019) to all data points shows the gas column density is positively proportional and then negatively proportional to the dust temperature when the dust is below and above $T_d^{trans} \simeq 37$ K, respectively. However, because the error bar is significantly large, we fit an upper envelope of the distribution and obtain a slightly higher value of $T_d^{trans} \simeq 40$ K. In the South, the transition temperature occurs around 37–39 K. However, the plot is much more scattered than that in the North.

In Figure 9, we show the relations of the polarization degree in three bands to the dust temperature (left panels from top to bottom). The black line shows the weighted-mean fit, and the black dashed line shows the piecewise line fit to the data. The separation owing to T_d-N_H is shown by two vertical dashed lines. The corresponding relations to the gas column density are shown in the middle and right panels, respectively. Notably, we only show the separation for $T_d^{trans} \simeq 37$ K here because the behavior is the same for any values between 37 and 40 K.

For $T_d \leqslant$ 37–40 K, in which the dust temperature and the gas column density both increase toward R136, the polarization degree rapidly increases, then decreases, and finally nearly plateaus with increasing dust temperature (region A in the left panels). Meanwhile, the polarization degree tends to decrease down to $N_H \sim 10^{21.7}$ cm^{-2} and plateaus with increasing gas column density (middle panels).

For $T_d >$ 37–40 K, in which the dust temperature and the gas column density are anticorrelated toward R136, the polarization degree first increases slightly and then decreases with increasing dust temperature (regions B and C in the left panels) and gas column density (right panels). Furthermore, the declining slope of $p-T_d$ is steeper for longer wavelengths, i.e., the mean slope of -0.52 at 89 μm, -0.72 at 154 μm, and -0.83 at 214 μm.

Similarly, Figure 10 shows the correlations of the polarization degree with the dust temperature and the gas column density in the South region. Although these plots are scattered, one can see a weak correlation between the polarization degree with the dust temperature. The relation with the gas column density is also separated into different ranges of dust temperature according to Figure 8. The relation with the gas column density looks somewhat similar to the middle and right panels of Figure 9. For $T_d <$ 37–39 K (middle panel), the polarization degree shows a monotonic decrease with increasing column density. However, for $T_d \geqslant$ 37–39 K (right panel), the polarization degree first increases and then decreases with increasing column density, as seen in the North region.

In summary, the $p-T_d$ and $p-N_H$ relations are not monotonic as in $p-I$. The most interesting feature is the anticorrelation of p versus T_d and the correlation of p with N_H, which cannot be explained by the basic RAT alignment theory alone.

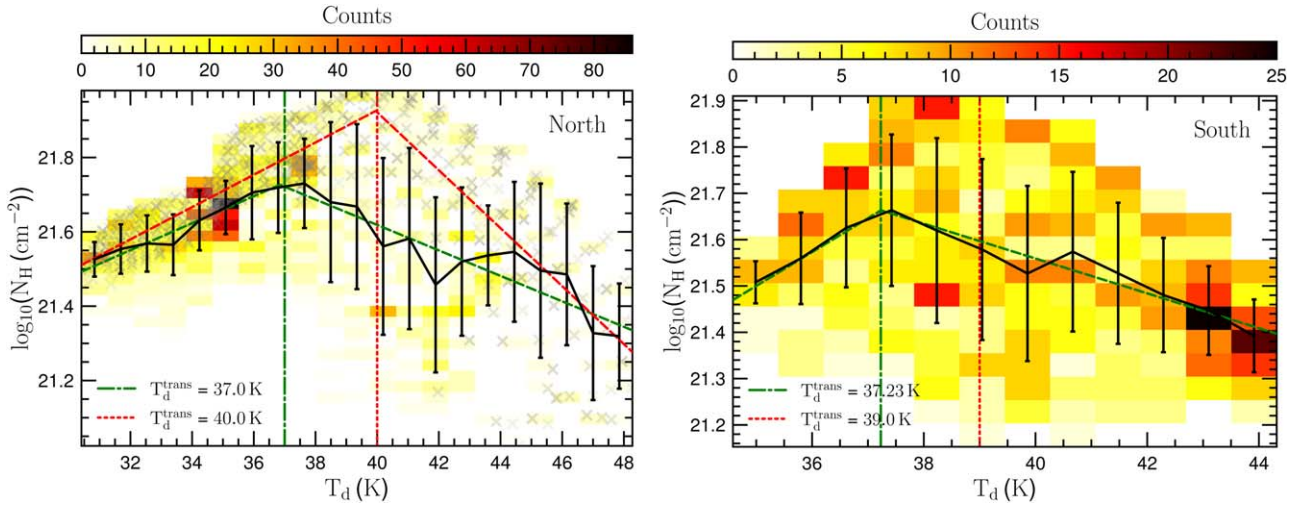

Figure 8. Relation of the gas column density and the dust temperature in the North region (left panel) and in the South region (right panel). They are positively correlated for $T_d < 37$ K, while they are negatively correlated for $T_d > 37$ K.

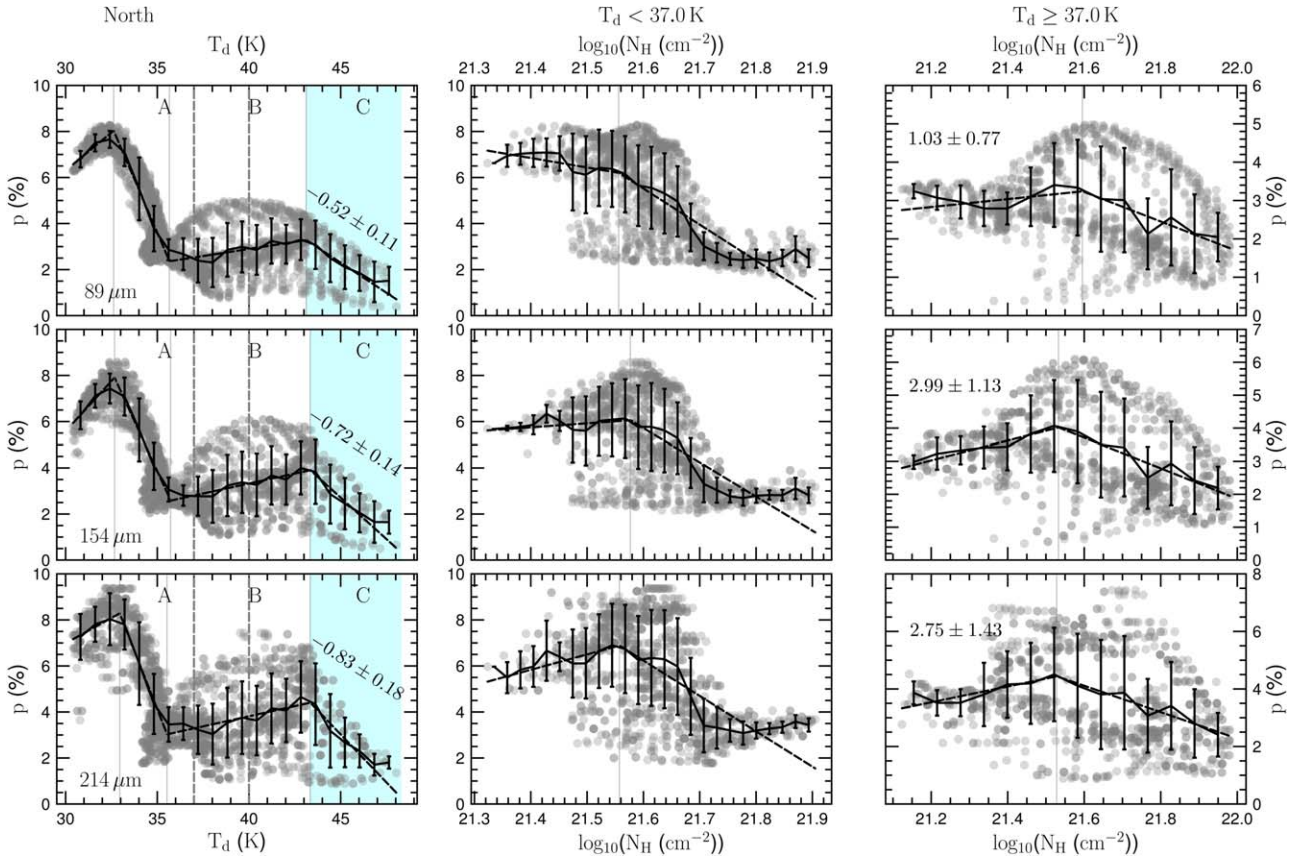

Figure 9. Left panel: correlation of the polarization degree with the dust temperature. Middle and right panels: correlation of the polarization to the gas column density within $T < 37$ K and $T_d \geqslant 37$ K, respectively. The solid black line is the weighted mean within the 1σ uncertainty in each bin. The dashed black line is the piecewise line fitting. On the left column, the dashed vertical lines indicate the corresponding T_d^{trans}. The $p-T_d$ relation shows three features: p decreasing (region A), slightly increasing (region B), and decreasing (region C) as T_d increases. The mean value of the slopes and their associated 95% level of confidences are given in region C.

4. Discussion

In this section, we will discuss the implications of the observed $p-I$, $p-T_d$, and $p-N_H$ relations for the leading theory of grain alignment and disruption based on RATs.

4.1. On the p–I *Relation and Grain Alignment*

The variation of the polarization degree of thermal dust emission with the total emission intensity (I) is a popular analysis of polarimetric data that provides information on grain alignment and magnetic fields. Numerous studies show that the polarization decreases with I as $p \propto I^{-\alpha}$ with the slope $\alpha \simeq 0-1$. If grain alignment and the magnetic field are uniform throughout the cloud, one expects $\alpha = 0$. If grain alignment only occurs in the outer layer and becomes completely lost in the inner region, one expects $\alpha = 1$ (Whittet et al. 2008). The latter slope was previously reported in the case of starless cores

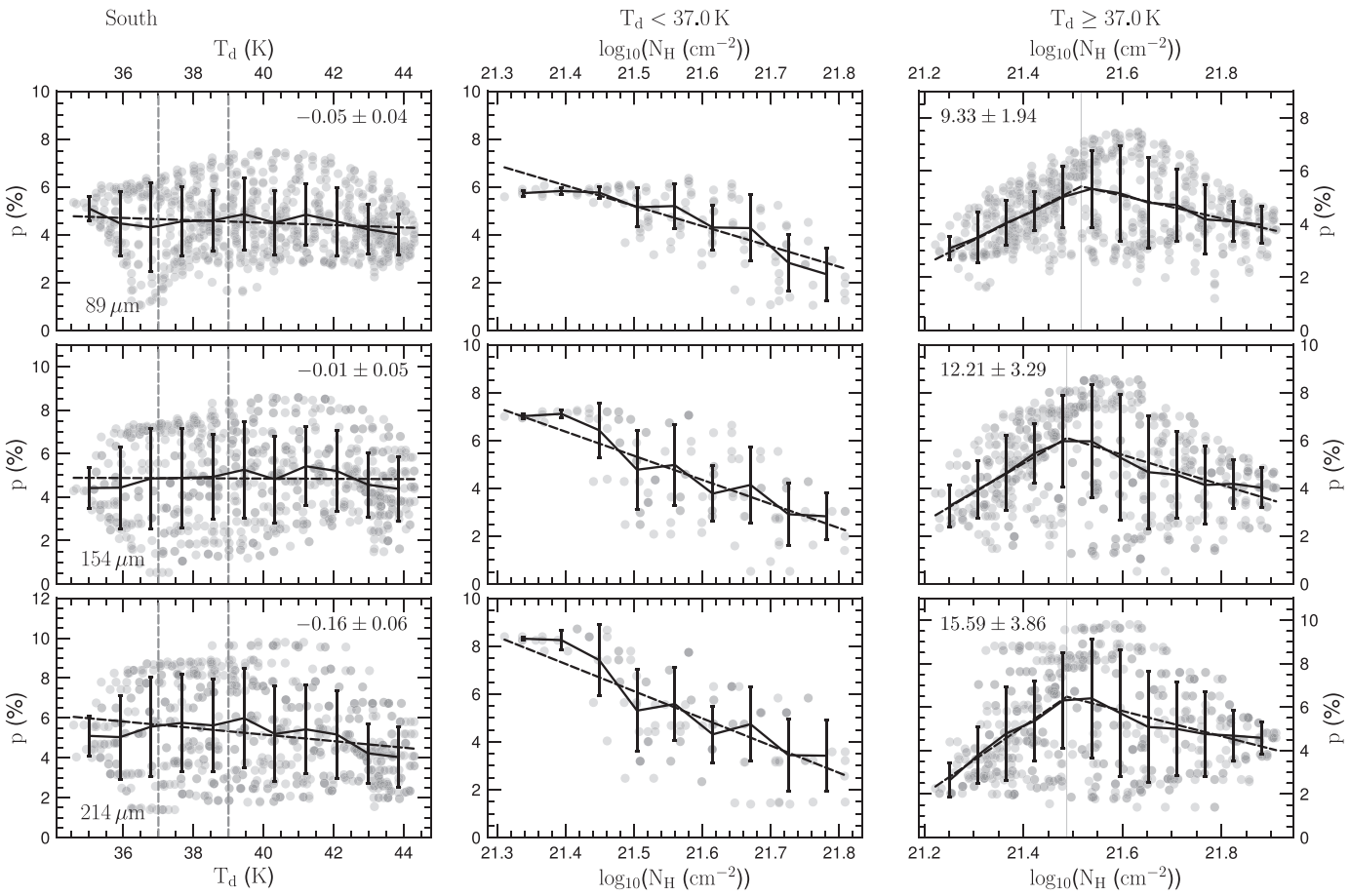

Figure 10. Similar to Figure 9, but for the South region. The polarization degree tends to decrease slowly with T_d (left panel). The polarization degree decreases with N_H for $T_d < 37$ K (middle panel), but it increases and decreases with N_H for $T_d > 37$ K (right panels).

(see, e.g., Crutcher et al. 2004; Alves et al. 2014; Jones et al. 2015). Theoretically, for uniform grain alignment in the cloud, the stochastic magnetic field is found to induce a slope of $\alpha = 0.5$ (see Jones et al. 1992, 2015).

In Section 3.2, we showed the $p-I$ diagrams in all three bands in both North and South regions. In the North, a single power-law fitting shows that the diagram at 89 μm has a steep slope of $\alpha > 0.5$, while the ones at longer wavelengths show a shallower slope of $\alpha < 0.5$. The slope of the $p-I$ relations seems rather low compared to other regions, e.g., the Auriga-California cloud ($\alpha \simeq 0.82$; Ngoc et al. 2021), Perseus B1 ($\alpha \simeq 0.8$; Coudé et al. 2019), Ophiuchus B, C ($\alpha \simeq 0.6-0.7$; Pattle et al. 2019), and Serpens South ($\alpha \simeq 0.55$; Pillai et al. 2020). A double power-law fitting indicates the diagrams change from the first, steep slope of $\alpha > 0.5$ to the second, shallower slope of $\alpha < 0.5$ toward the peak dust emission intensity. This transition feature seems similar to the case of NGC 6334 (Arzoumanian et al. 2021). In both cases, the shallow slope of the $p-I$ diagram is shown, which can be explained by the high grain alignment efficiency of RATs owing to the intense radiation flux from the luminous source R136.

Indeed, according to the RAT alignment theory, the degree of dust polarization is determined by the minimum size of aligned grains (a_{align}). A smaller value of a_{align} results in a higher p because the size distribution of aligned grains (i.e., from a_{align} to the maximum grain size a_{max}) is broader. Similarly, a larger value of a_{align} causes the lower polarization due to the narrower size distribution of aligned grains, assuming that a_{max} is fixed (without RATD). The alignment size depends on the local physical conditions as $a_{align} \sim n_H^{2/7} T_d^{-12/7}$ (see Appendix A).

Because 30 Dor is a complex region, it is very difficult to accurately constrain the local physical properties such as n_H and T_d (see Okada et al. 2019). Therefore, in Figure 11, we show the map of a_{align} with respect to T_d and n_H. The values of n_H span broadly from 10^3 to 10^6 cm^{-3} (see Chevance et al. 2016 and Lee et al. 2019), while those of T_d are adopted from observations (Figure 3(d)). The alignment size increases with increasing gas density and decreasing dust temperature (from the upper-left corner to the lower-right corner). For a given dust temperature, a_{align} becomes larger for higher gas density (from the left panel to the right panel), which arises from the increase of the collisional disalignment rate with the gas density.

In the case of two slopes, when approaching the luminous source of R136, the local dust temperature (i.e., radiation strength) increases, which significantly decreases a_{align} (see Figure 11). As a result, the polarization degree of thermal dust emission increases (Hoang et al. 2021). This can reproduce the shallow slope of $\alpha \sim 0.3$–0.4 observed toward the peak intensity. For the first steep slope of $\alpha > 0.5$, the alignment size increases due to the decrease of the ISRF, as well as collisional damping becoming more significant, and one expects the slope of $\alpha = 1$ when grain alignment is completely

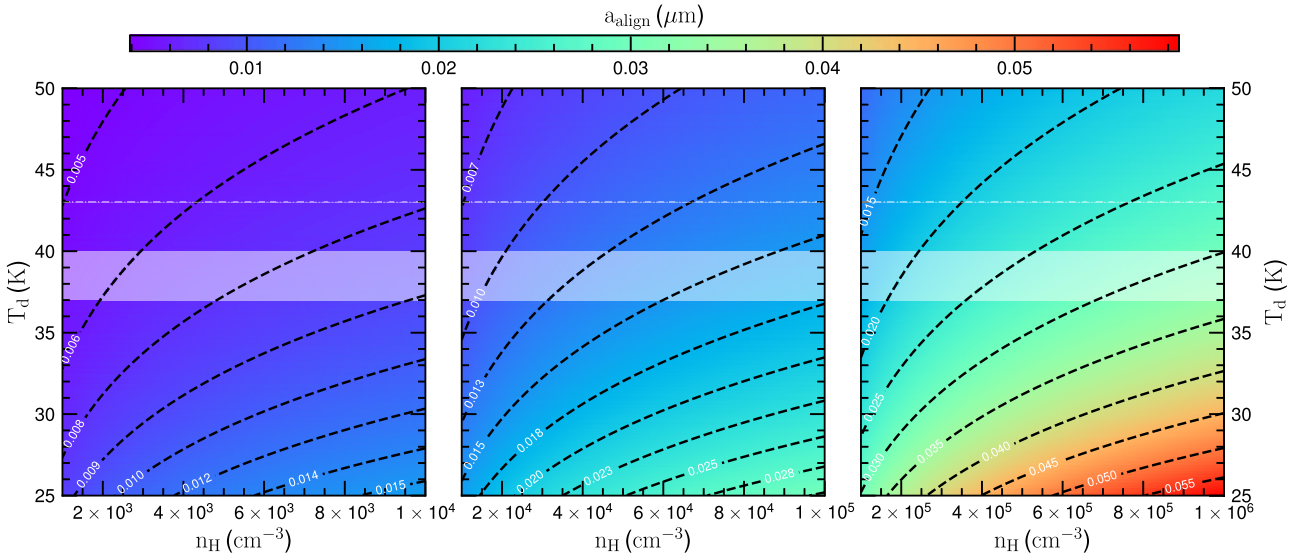

Figure 11. The alignment size (minimum size of aligned grains by RATs, $a_{\rm align}$) as functions of the dust temperature ($T_{\rm d}$) and the gas volume density ($n_{\rm H}$) computed with $\bar{\lambda} = 0.3$, $\gamma = 1$, and $T_{\rm gas} = T_{\rm d}$. The alignment size is larger (smaller) for higher (lower) gas density and lower (higher) dust temperature. The white region shows the range of the transition temperature ($T_{\rm d}^{\rm trans}$).

lost. However, if grain growth occurs, the size distribution of aligned grains ($a \sim a_{\rm align} - a_{\rm max}$) is still finite, which can produce a slope shallower than $\alpha \sim 1$ (see Hoang et al. 2021). Incidentally, the optical to near-infrared observations of 30 Dor by the Hubble Space Telescope (De Marchi & Panagia 2014) reported a high value of the ratio of the total to selective extinction $R_{\rm V}$ as 4.4, which implies grain growth in 30 Dor. Other effects, including the tangling of the magnetic fields, can also reproduce the first slope.

In the South, the p–I diagrams illustrate two clusters with different properties. The first group shows a quite shallow slope with $\alpha \simeq 0.2$–0.5 at around the peak of the intensity and gas column density, which is opposite to that in the North. The second group otherwise shows a very deep slope as $\alpha \simeq 1$. Naturally, the contradiction in polarization degree reflects a difference in the radiation flux and grain size distribution. However, the dust temperature is not the highest in dense gas (Figure 3(d)). Thus, it is likely that grains are larger in the dense region and responsible for the shallow slope of the p–I diagram.

The North and South regions share a common feature where the polarization degree seems to be larger at greater distances from the central source with a low gas density and low dust temperature. An interesting feature is that the polarization degree appears to be low in the vicinity of R136, in which the radiation is strong and the gas density is not densest (Figure 3(c)). This is evidence in support of the RATD mechanism, which will be discussed in detail in Section 4.3.

4.2. On the p–T_d and p–N_H Relations and Grain Alignment

As shown in Figure 9, the variation of p with $T_{\rm d}$ and $N_{\rm H}$ in the North region is more complex than the p–I relation. For $T_{\rm d} \leqslant 37$ K, p decreases with increasing $T_{\rm d}$ (left panels) and $N_{\rm H}$ (middle panels). For $T_{\rm d} > 37$ K, p first increases with increasing $T_{\rm d}$ and $N_{\rm H}$, then decreases when $T_{\rm d}$ becomes sufficiently large (see the B and C regions in the left panels). The increase of p with $T_{\rm d}$ and the decrease of p with $N_{\rm H}$ are expected from the RAT alignment theory as the alignment size decreases with increasing U and decreasing $n_{\rm H}$ (see Figure 11, also Appendix A. However, the decrease of p with $T_{\rm d}$ is unexpected from the basic RAT alignment theory because the alignment size $a_{\rm align}$ is smaller for larger $T_{\rm d}$ (U). Similarly, the increase of p with $N_{\rm H}$ is unexpected because $a_{\rm align}$ increases with the gas density.

In the South, the relations of p to $T_{\rm d}$ and $N_{\rm H}$ are more scattered and not very obvious as shown in Figure 10. However, the South is likely closer to R136 than the North, and the selected area covers mostly the region where the grain alignment efficiency is high. However, the polarization degree does not seem to vary with $T_{\rm d}$ and decreases with decreasing gas column density for $T_{\rm d} > T_{\rm d}^{\rm trans}$. As in the North, the latter trend is opposite to the expectation from the basic RAT alignment theory.

4.3. New Evidence of the RATD Mechanism

In Figures 9 and 10, we found that the polarization degree first increases and then decreases as the dust temperature increases and the gas column density decreases (region C in Figure 9) for $T_{\rm d} > 43$ K. The decrease of p with $T_{\rm d}$ (higher radiation flux, closer to R136) and the increase of p with decreasing $N_{\rm H}$ cannot be explained by the basic RAT alignment theory, as discussed in the previous subsection unless the increased dust heating is associated with the increase in the tangling of the magnetic field. Below, we suggest that the combination of the RAT alignment with the RATD mechanism (Hoang et al. 2019) can reproduce this feature.

According to the RATD mechanism, dust grains subject to a strong radiation field (i.e., close to the source R136) can be spun up to extremely fast rotation. The induced centrifugal stress due to grain suprathermal rotation can exceed the tensile strength of the grain material, resulting in the spontaneous fragmentation of large grains into smaller ones. The depletion of large grains causes the decrease in the thermal dust polarization degree at long wavelengths (see Lee et al. 2020; Tram et al. 2021a).

To study if RATD can reproduce the observed anti-correlation of p–$T_{\rm d}$, let us estimate the critical size above which dust grains are disrupted, $a_{\rm disr}$. The disruption size

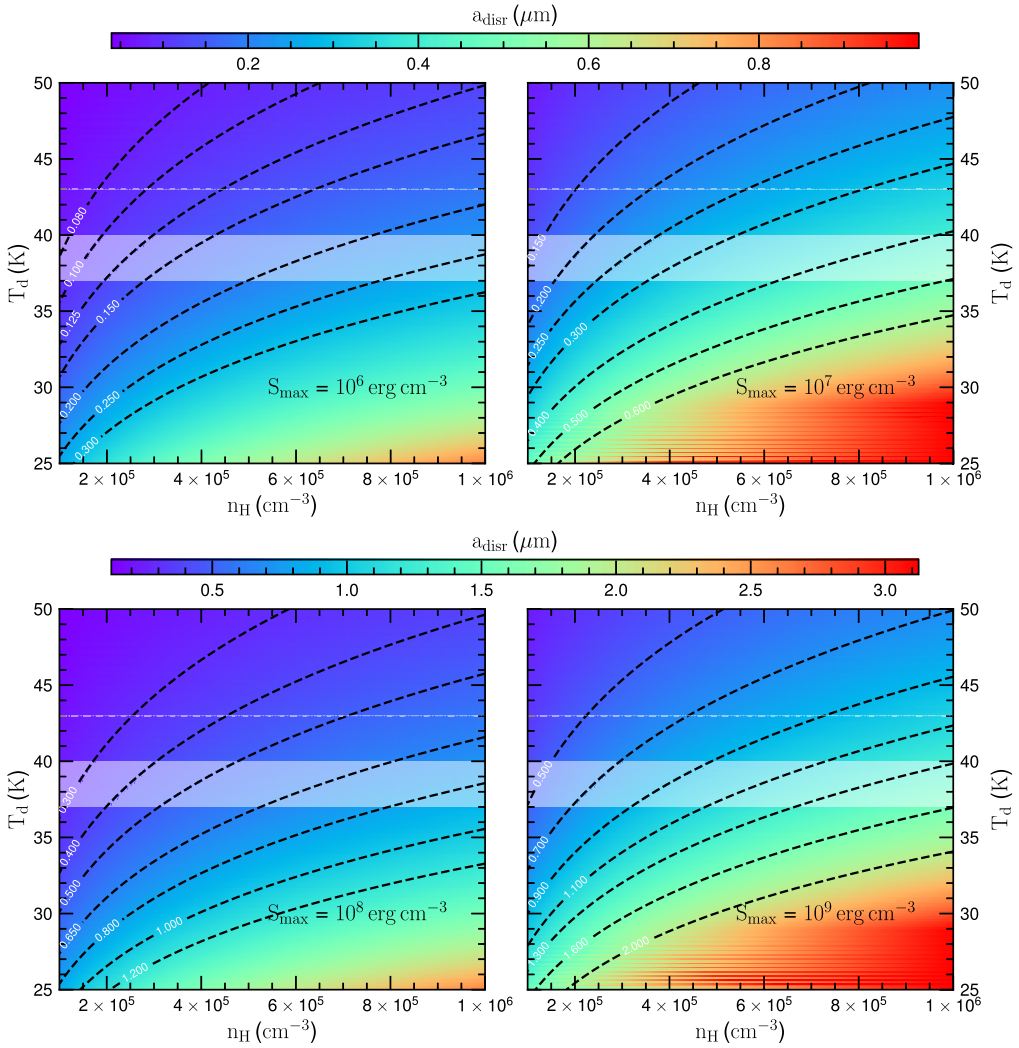

Figure 12. Similar to Figure 11 but for the grain disruption size (a_{align}) for different values of the tensile strength (S_{max}). a_{disr} is smaller (larger) for higher (lower) T_d and lower (higher) n_H. For the same physical condition, a_{disr} is larger for higher S_{max}. In each panel, the white dashed horizontal line represents $T_d = 43$ K.

depends on the local conditions and the grain structure as $a_{disr} \sim n_H^{1/2} T_d^{-3} S_{max}^{1/4}$ (see Appendix B). As shown in Tram et al. (2021a, 2021b), the disruption occurs at the critical disruption temperature of $T_d^{disr} \simeq 32$ K for $n_H \simeq 10^5$ cm^{-3} and $T_d^{disr} \simeq 71$ K for $n_H \sim 10^6$ cm^{-3}. Thus, the gas volume density in the region within $43 \leqslant T_d < 50$ K could be in (10^5–10^6 cm^{-3}) interval. Figure 12 shows the map of the grain disruption size as a function of T_d and n_H for different values of S_{max}. Large grains within the composite structure ($S_{max} \sim 10^5$–10^7 erg cm^{-3}) are being disrupted more than more-compact grains (higher value of S_{max}). For instance, for $n_H = 6 \times 10^5$ cm^{-3} and $T_d = 43$ K, $a_{dirs} = 0.15$, 0.26, 0.46, and 0.82 μm for $S_{max} = 10^6$, 10^7, 10^8, and 10^9 erg cm^{-3}, respectively. Thus, the RATD mechanism can reasonably disrupt the composite grains for $T_d \geqslant 43$ K. The disruption size gets smaller for higher T_d.

Figure 13 sketches our understanding of the main feature of dust polarization in 30 Dor expected from theoretical modeling of dust polarization based on grain alignment and disruption by RATs (Lee et al. 2020). For an illustration, a color map of a_{align} (in arbitrary units) is shown as functions of T_d and n_H. The feature of p fundamentally depends on the T_d–n_H relation. If we assume $n_H \sim N_H$ maps (e.g., the local variation of the cloud depth is significantly small or negligible), the observed polarization degree (p) profile could be explained in three ranges of T_d.

For $T_d < T_d^{trans}$ (at which the T_d–n_H relation changes sign from positive to negative; see Figure 8), T_d is positively correlated to n_H. If the gas density increases faster than the radiation strength ($U \propto T_d^6$), such that the rotational damping by gas collisions is sufficiently strong to prevent the grains from being spun up to the disruption limit by RATs, a_{align} is larger with increasing T_d and n_H (solid white arrow). This increment of a_{align} consequently causes the polarization degree to decrease to both the dust temperature and gas density as expected from the RAT alignment theory. In this case, a_{align} might also become constant with a specific range of T_d and n_H because of their opposite effects. These features explain the observed region A in p–T_d in Figure 9 and p–N_H in the middle panel of Figures 9 and 10. In the case where the dust temperature increases such that U increases faster than the gas density, the rotational damping by gas collisions is insufficiently strong to prevent the grains from being spun up by RATs, a_{align} is getting smaller as T_d and n_H increase. Thus, the polarization degree is increasing instead of decreasing, which contradicts the observed trend of 30 Dor.

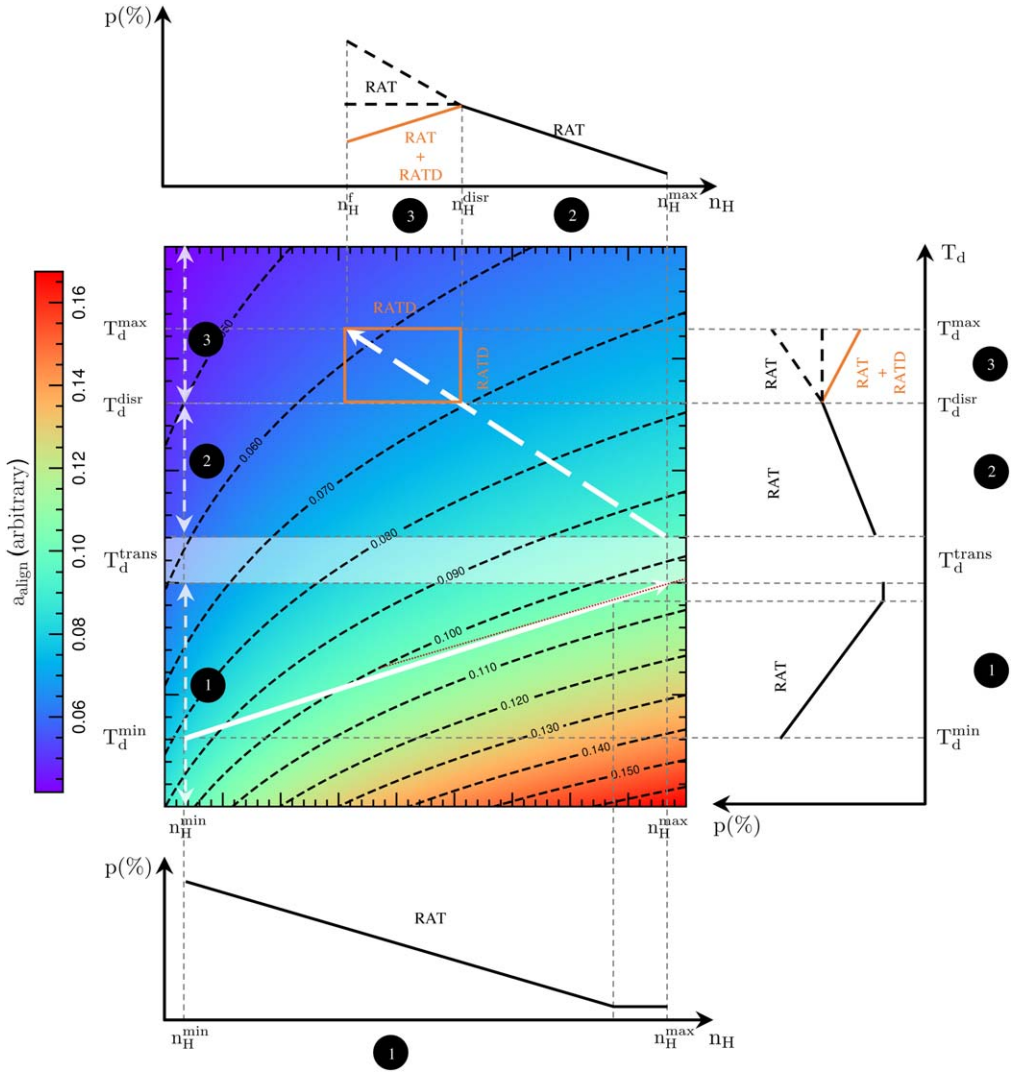

Figure 13. Understanding the thermal dust polarization in 30 Dor in light of RAT alignment and RATD. According to the RAT alignment theory, the polarization degree is determined by the grain alignment size ($a_{\rm align}$), which depends on the dust temperature ($T_{\rm d}$) and the gas volume density ($n_{\rm H}$). Therefore, the observed $p-T_{\rm d}$ and $p-N_{\rm H}$ trends could be explained by three distinct stages denoted by the circled numbers 1, 2, and 3. For 1 with $T_{\rm d} < T_{\rm d}^{\rm trans}$, $T_{\rm d}$ is positively proportional to $n_{\rm H}$ (solid white arrow); the grain alignment size increases along this direction only if $n_{\rm H}$ increases faster than the radiation strength $U \propto T_{\rm d}^6$, which results in the decrease in the polarization degree (p) with both $T_{\rm d}$ and $n_{\rm H}$. If $T_{\rm d}$ increases such that U increases faster than $n_{\rm H}$, one expects p to go up. For 2 with $T_{\rm d} > T_{\rm d}^{\rm trans}$, $T_{\rm d}$ is negatively proportional to $n_{\rm H}$ (dashed white arrow), p increases with increasing $T_{\rm d}$ and decreasing $n_{\rm H}$ as $a_{\rm align}$ becomes smaller along this direction. Finally, for 3 with $T_{\rm d} > T_{\rm d}^{\rm disr}$, the RATD effect becomes active, resulting in the drop of p toward higher $T_{\rm d}$ and lower $n_{\rm H}$ (orange lines), which explains the observed trend. Without RATD, p is expected to continue increasing or be constant. Therefore, the joint effect of grain alignment and disruption by RATs can successfully explain the observed polarized thermal dust emission of 30 Dor.

For $T_{\rm d} > T_{\rm d}^{\rm trans}$, $T_{\rm d}$ and $n_{\rm H}$ are anticorrelated (see Figure 8). The gas collision damping is further weakened; the grain alignment size gets smaller as $T_{\rm d}$ increases (dashed white arrow). Thus, the polarization degree increases toward higher $T_{\rm d}$ and lower $n_{\rm H}$. This feature could explain region B observed in the $p-T_{\rm d}$ diagram in Figure 9.

For $T_{\rm d} > T_{\rm d}^{\rm disr}$, the depletion of large grains due to the RATD mechanism results in the decrease of the polarization degree toward higher $T_{\rm d}$ and lower $n_{\rm H}$. This feature successfully reproduces the observed $p-T_{\rm d}$ in region C of Figure 9 and $p-N_{\rm H}$ in the right panels of Figures 9 and 10. Otherwise, the polarization degree is expected to continuously increase or at least flatten according to the RAT alignment theory (see Lee et al. 2020).

However, the question remains why the relation between p and $T_{\rm d}$ is weak in the South. This slow variation may be due to the saturation of RATD, which occurs when $T_{\rm d} \gg T_{\rm disr}$ (see Figure 14 in Lee et al. 2020). Induced small grains likely have compact structures, and RATD ceases to act at some high $T_{\rm d}$. Furthermore, when $T_{\rm d}$ is large, IR damping is so strong that $a_{\rm disr}$ becomes slow to change with $T_{\rm d}$. Both effects induce the slow variation of p with $T_{\rm d}$.

Previous studies have reported the anticorrelation of dust polarization with grain temperature for several molecular clouds (Planck Collaboration et al. 2020), ρ Ophiuchus A, which is irradiated by a nearby B-association star (Santos et al. 2019; Tram et al. 2021a),[8] and a cloud surrounding the massive star BN/KL (Tram et al. 2021b). Numerical modeling studies (Lee et al. 2020) show that the RATD mechanism (Hoang 2020) could successfully reproduce the observed anticorrelation of the polarization with grain temperature at

[8] In the case of ρ Ophiuchus A, the observed trend of $p-T_{\rm d}$ is explained by processes 2 and 3 in Figure 13.

the same far-IR and submillimeter wavelength ranges. The observed anticorrelation of $p-T_{\rm d}$ in 30 Dor is new evidence for the RATD mechanism.

4.4. Dust Polarization Mechanisms

Our analysis so far focused on the polarization degree with the assumption that far-IR dust polarization is induced by dust grains aligned with a preferred direction. The modern theory of RAT alignment theory implies that such a preferred axis could be the magnetic field (B-RAT) or the radiation direction (k-RAT) (Lazarian & Hoang 2007). As a result, the polarization vectors of polarized thermal emission are perpendicular to the magnetic field (radiation direction). The B-RAT alignment is most likely in the diffuse ISM and molecular clouds, whereas the k-RAT can occur near a strong radiation source where the rate of grain precession around the radiation direction is larger than the Larmor precession around the magnetic field (Hoang & Lazarian 2016; Lazarian & Hoang 2019). In this case, the polarization vectors of thermal dust emission are perpendicular to the radiation direction. Therefore, the polarization vectors provide valuable constraints on dust magnetic properties and alignment mechanisms (Chuss et al. 2019; Lazarian & Hoang 2019; Pattle et al. 2021).

In the South region of Figure 2, the polarization vectors (the E vectors) appear to be concentric with respect to the intense source R136. Such a polarization pattern is different from the one in the North region, which is far from the source R136 where grains are most likely aligned via B-RAT. This indicates that the alignment mechanisms in the South may be due to the alignment with the radiation direction. Evidence for k-RAT is previously reported for some star-forming regions (Chuss et al. 2019; Pattle et al. 2021) and protoplanetary disks (Kataoka et al. 2017; Stephens et al. 2017). We will study in detail this issue in a follow-up paper on 30 Dor.

5. Summary

In this paper, we report our results analyzing the far-IR polarimetric observations of 30 Doradus by SOFIA/HAWC+. The 30 Dor cloud is located in the LMC and mainly irradiated by an intense radiation source from the massive R136 cluster. Thus, this region is an ideal target to study the physics of grain alignment and disruption driven by RATs. To infer the alignment and disruption properties of dust grains, we performed three different analyses based on the polarization degree, including $p-I$, $p-N_{\rm H}$, and $p-T_{\rm d}$. Our main findings are summarized as follows:

1. The thermal dust polarization varies across the 30 Dor cloud, in which there are two main regions, namely North and South, relative to the massive star cluster R136. In the North region, the polarization patterns are likely radial from R136 within the peak polarization angle at $\simeq 20^\circ$, while they are concentric around R136 within the peak polarization angle of $\simeq -60^\circ$ in the South region.
2. For the North region, a single power-law fitting shows a shallow slope of the $p-I$ diagrams, which could be explained by an intense radiation field. A double power-law fitting shows a change from a steeper slope of $\alpha > 0.5$ to a shallower slope as $\simeq I^{-0.4}-I^{-0.3}$ toward higher intensity. The latter shallow slope most likely arises from the enhanced alignment of grains by RATs when approaching the source R136.
3. The variations of the polarization degree with the dust temperature and gas column density in the North are complex. The polarization degree decreases with increasing dust temperature and gas column density for $T_{\rm d} < 37$ K, which might result from the loss of grain alignment due to strong collisional damping by denser gas. For $T_{\rm d} > 37$ K, the polarization degree increases as the dust temperature increases and the gas column density decreases. However, the polarization degree decreases as the dust temperature increases beyond ~ 43 K, and the gas column density further decreases. Such an anticorrelation of $p-T_{\rm d}$ is consistent with the prediction of the RATD theory that the dust polarization decreases due to the disruption of large grains toward the intense radiation source R136.
4. In the South region, the polarization degree is higher, and the $p-I$ slope is shallower at the peak of the intensity and gas column density, whereas the polarization degree is the highest farther away (low intensity and less dense gas) and decreases steeply as $p \propto I^{-1}$ backward to R136 (higher intensity and denser gas). The first feature is likely caused by the enhancement of grain alignment by RATs due to the radiation from the source R136. The second feature is unexpected from the basic RAT alignment theory but is consistent with the prediction by the RATD effect, as in the North.
5. In the South, the stronger grain randomization by gas collisions in the densest part results in a weak correlation of the polarization degree with the dust temperature, whereas the polarization degree likely decreases toward low and high gas column density. However, the relations are quite scattered and show a large error bar.

The values of the dust temperature and gas column density used in this work are derived from the modified blackbody fitting to the Herschel data, and they thus encompass the projection effect. Our conclusions are given without taking the B-field tangling into account. The variation of the magnetic field could result in the modification of the grain alignment and then the polarization degree. Despite these, our SOFIA/HAWC+ data show that the grain alignment is complicated and significantly varies across the 30 Dor cloud, and is evidence of the strong impact of the intense radiation field of the massive star cluster R136. The drop in polarization degree close to the central source, in which the gas column density is not peaked, is contrary to the RAT alignment theory. The lower abundance of large grains via the disruption mechanism by radiative torque could be responsible for this declination.

We thank the anonymous referee for a helpful report. This research is based on observations made with the NASA/DLR Stratospheric Observatory for Infrared Astronomy (SOFIA). SOFIA is jointly operated by the Universities Space Research Association, Inc. (USRA), under NASA contract NNA17BF53C, and the Deutsches SOFIA Institut (DSI) under DLR contract 50 OK 0901 to the University of Stuttgart. Financial support for this work was provided by NASA through award 4_0152 issued by USRA. T.H. is funded by the National Research Foundation of Korea (NRF) grant funded by the Korea government (MSIT) through the Mid-career

Research Program (2019R1A2C1087045). A.S. and B-G.A. are supported by NSF Grant-1715876.

Facility: SOFIA.

Appendix A
Grain Alignment Size

Grains are effectively aligned only when they can rotate suprathermally, i.e., the grain angular velocity (ω) is greater than the thermal velocity (ω_T) (Hoang & Lazarian 2008, 2016). The minimum alignment size ($a_{\rm align}$) above which grains are aligned can be computed as $\omega(a_{\rm align}) \equiv 3 \times \omega_T$. When exposed to a radiation source, the minimum $a_{\rm align}$ is determined analytically as (see Equation (26) in Hoang et al. 2021)

$$a_{\rm align} \simeq 0.055\hat{\rho}^{-1/7}\left(\frac{\gamma}{0.1}\right)^{-2/7}\left(\frac{n_{\rm H}}{10^3{\rm cm}^{-3}}\right)^{2/7}U^{-2/7} \times \left(\frac{T_{\rm gas}}{10{\rm K}}\right)^{2/7}\left(\frac{\bar{\lambda}}{1.2\mu{\rm m}}\right)^{4/7}(1+F_{\rm IR})^{2/7}\,\mu{\rm m}, \quad \text{(A1)}$$

where γ is the anisotropy degree, $\bar{\lambda}$ is the mean wavelength, and U[9] is the strength of the radiation field. $n_{\rm H}$ and $T_{\rm gas}$ are the number density and temperature of the gas. $F_{\rm IR}$ is the ratio of the IR damping to the collisional damping rate. If we use $U \simeq (T_{\rm d}/16.4\ {\rm K})^6$ (Draine & Weingartner 2011), one can see that the alignment size depends on the local properties as $a_{\rm align} \sim n_{\rm H}^{2/7}T_{\rm d}^{-12/7}$. The alignment size decreases (increases) with decreasing (increasing) gas density and increasing (decreasing) dust temperature as shown in Figure 11.

Appendix B
Grain Disruption Size

Large grains exposed to an intense radiation field can be spun up and become extremely fast by RATs. The fast rotation induces a strong centrifugal stress that opposes the binding energy that holds up the grain structure (i.e., tensile strength). Once the centrifugal stress exceeds the tensile strength, the grain is spontaneously fragmented. This fragmentation is called RATD. The critical grain size above which grains will be disrupted by the RATD mechanism is

$$a_{\rm disr} \simeq 0.22\hat{\rho}^{-1/4}\gamma^{-1/2}\left(\frac{n_{\rm H}}{10^3{\rm cm}^{-3}}\right)^{1/2}U^{-1/2}\left(\frac{T_{\rm gas}}{10{\rm K}}\right)^{1/4} \times \left(\frac{\bar{\lambda}}{0.5\mu{\rm m}}\right)\left(\frac{S_{\rm max}}{10^7{\rm ergcm}^{-3}}\right)^{1/4}(1+F_{\rm IR})^{1/2}\,\mu{\rm m}, \quad \text{(B1)}$$

where $S_{\rm max}$ is the tensile strength that is determined by the internal structure of dust grains (see Equation (30) in Hoang et al. 2021). The compact grains have a higher tensile strength and are stronger than the composite ones (see Hoang 2019). One can see that $a_{\rm disr} \sim n_{\rm H}^{1/2}T_{\rm d}^{-3}S_{\rm max}^{1/4}$, which illustrates that the disruption size also decreases (increases) with decreasing (increasing) gas density and increasing (decreasing) dust temperature. Moreover, at the same local condition, grains within a weaker structure are easier to disrupt than those with a stronger structure, as shown in Figure 12.

[9] $U = u_{\rm rad}/u_{\rm ISRF}$, with $u_{\rm rad} = \int u_\lambda d\lambda$, the radiation energy density of the local radiation field, and $u_{\rm ISRF} \approx 8.64 \times 10^{-13}$ erg cm^{-3}, the radiation energy density of the local ISRF (Mathis et al. 1983).

ORCID iDs

Le Ngoc Tram https://orcid.org/0000-0002-6488-8227
Thiem Hoang https://orcid.org/0000-0003-2017-0982
Enrique Lopez-Rodriguez https://orcid.org/0000-0001-5357-6538
Simon Coudé https://orcid.org/0000-0002-0859-0805
Archana Soam https://orcid.org/0000-0002-6386-2906
B-G Andersson https://orcid.org/0000-0001-6717-0686
Min-Young Lee https://orcid.org/0000-0002-9888-0784
William D. Vacca https://orcid.org/0000-0002-9123-0068
Hyeseung Lee https://orcid.org/0000-0003-3465-3213

References

Alves, F. O., Frau, P., Girart, J. M., et al. 2014, A&A, 569, L1
Andersson, B. G., Lazarian, A., & Vaillancourt, J. E. 2015, ARA&A, 53, 501
Arzoumanian, D., Furuya, R., Hasegawa, T., et al. 2021, A&A, 647, A78
Bernard, J.-P., Reach, W. T., Paradis, D., et al. 2008, AJ, 136, 919
Chevance, M., Madden, S. C., Lebouteiller, V., et al. 2016, A&A, 590, A36
Chuss, D. T., Andersson, B.-G., Bally, J., et al. 2019, ApJ, 872, 187
Coudé, S., Bastien, P., Houde, M., et al. 2019, ApJ, 877, 88
Crutcher, R. M., Nutter, D. J., Ward-Thompson, D., & Kirk, J. M. 2004, ApJ, 600, 279
De Marchi, G., & Panagia, N. 2014, MNRAS, 445, 93
De Marchi, G., Paresce, F., Panagia, N., et al. 2011, ApJ, 739, 27
Dolginov, A. Z., & Mytrophanov, I. G. 1976, Ap&SS, 43, 257
Draine, B. T. 2011, Physics of the Interstellar and Intergalactic Medium (Princeton, NJ: Princeton Univ. Press)
Draine, B. T., & Weingartner, J. C. 1996, ApJ, 470, 551
Dufour, R. J., Shields, G. A., & Talbot, R. J. J. 1982, ApJ, 252, 461
Fissel, L. M., Ade, P. A. R., Angilè, F. E., et al. 2016, ApJ, 824, 134
Galliano, F., Madden, S. C., Tielens, A. G. G. M., Peeters, E., & Jones, A. P. 2008, ApJ, 679, 310
Gordon, K. D., Roman-Duval, J., Bot, C., et al. 2014, ApJ, 797, 85
Gordon, M. S., Lopez-Rodriguez, E., Andersson, B. G., et al. 2018, arXiv:1811.03100
Harper, D. A., Runyan, M. C., Dowell, C. D., et al. 2018, JAI, 7, 1840008
Hoang, T. 2019, ApJ, 876, 13
Hoang, T. 2020, Galax, 8, 52
Hoang, T., & Lazarian, A. 2008, MNRAS, 388, 117
Hoang, T., & Lazarian, A. 2016, ApJ, 831, 159
Hoang, T., Tram, L. N., Lee, H., & Ahn, S.-H. 2019, NatAs, 3, 766
Hoang, T., Tram, L. N., Lee, H., Diep, P. N., & Ngoc, N. B. 2021, ApJ, 908, 218
Indebetouw, R., de Messières, G. E., Madden, S., et al. 2009, ApJ, 694, 84
Jekel, C. F., & Venter, G. 2019, pwlf: A Python Library for Fitting 1D Continuous Piecewise Linear Functions v0.4.1, GitHub, https://github.com/cjekel/piecewise_linear_fit_py
Jones, T. J., Bagley, M., Krejny, M., Andersson, B. G., & Bastien, P. 2015, AJ, 149, 31
Jones, T. J., Klebe, D., & Dickey, J. M. 1992, ApJ, 389, 602
Kataoka, A., Tsukagoshi, T., Pohl, A., et al. 2017, ApJL, 844, L5
Lazarian, A. 2007, JQSRT, 106, 225
Lazarian, A., Andersson, B.-G., & Hoang, T. 2015, in Polarimetry of Stars and Planetary Systems, ed. L. Kolokolova, J. Hough, & A. Levasseur-Regourd (Cambridge: Cambridge Univ. Press), 81
Lazarian, A., & Hoang, T. 2007, MNRAS, 378, 910
Lazarian, A., & Hoang, T. 2019, ApJ, 883, 122
Lee, H., Hoang, T., Le, N., & Cho, J. 2020, ApJ, 896, 44
Lee, M. Y., Madden, S. C., Le Petit, F., et al. 2019, A&A, 628, A113
Lopez, L. A., Krumholz, M. R., Bolatto, A. D., Prochaska, J. X., & Ramirez-Ruiz, E. 2011, ApJ, 731, 91
Mathis, J. S., Mezger, P. G., & Panagia, N. 1983, A&A, 500, 259
Medan, I., & Andersson, B. G. 2019, ApJ, 873, 87
Meixner, M., Panuzzo, P., Roman-Duval, J., et al. 2013, AJ, 146, 62
Newville, M., Stensitzki, T., Allen, D. B., & Ingargiola, A. 2014, LMFIT: Non-Linear Least-Square Minimization and Curve-Fitting for Python, v0.8.0, Zenodo, doi:10.5281/zenodo.11813
Ngoc, N. B., Diep, P. N., Parsons, H., et al. 2021, ApJ, 908, 10

Okada, Y., Güsten, R., Requena-Torres, M. A., et al. 2019, A&A, 621, A62
Pattle, K., Lai, S.-P., Hasegawa, T., et al. 2019, ApJ, 880, 27
Pattle, K., Lai, S.-P., Wright, M., et al. 2021, MNRAS, 503, 3414
Pedregosa, F., Varoquaux, G., Gramfort, A., et al. 2011, J. Mach. Learn. Res., 12, 2825
Pillai, T. G. S., Clemens, D. P., Reissl, S., et al. 2020, NatAs, 4, 1195
Planck Collaboration, Aghanim, N., Akrami, Y., et al. 2020, A&A, 641 A12
Reissl, S., Wolf, S., & Brauer, R. 2016, A&A, 593, A87
Roman-Duval, J., Gordon, K. D., Meixner, M., et al. 2014, ApJ, 797, 86
Santos, F. P., Chuss, D. T., Dowell, C. D., et al. 2019, ApJ, 882, 113
Soam, A., Andersson, B. G., Acosta-Pulido, J., et al. 2021a, ApJ, 907, 93
Soam, A., Andersson, B. G., Straižys, V., et al. 2021b, AJ, 161, 149
Stephens, I. W., Yang, H., Li, Z.-Y., et al. 2017, ApJ, 851, 55
Tram, L. N., Hoang, T., Lee, H., et al. 2021a, ApJ, 906, 115
Tram, L. N., Lee, H., Hoang, T., et al. 2021b, ApJ, 908, 159
Vaillancourt, J. E., Andersson, B. G., Clemens, D. P., et al. 2020, ApJ, 905, 157
Whittet, D. C. B., Hough, J. H., Lazarian, A., & Hoang, T. 2008, ApJ, 674, 304